The 2D Analytic Signal on
RF and B-Mode Ultrasound Images

Christian Wachinger, Tassilo Klein, and Nassir Navab

Computer Aided Medical Procedures (CAMP), TUM, Munich, Germany

Abstract. The fundamental property of the analytic signal is the split of identity, meaning the separation of quantitative and qualitative information in form of the local phase and the local amplitude, respectively. Especially the structural representation, independent of brightness and contrast, of the local phase is interesting for numerous image processing tasks. Recently, the extension of the analytic signal from 1D to 2D, covering also intrinsic 2D structures, was proposed. We show the advantages of this improved concept on ultrasound RF and B-mode images. Precisely, we use the 2D analytic signal for the envelope detection of RF data. This leads to advantages for the extraction of the information-bearing signal from the modulated carrier wave. We illustrate this, first, by visual assessment of the images, and second, by performing goodness-of-fit tests to a Nakagami distribution, indicating a clear improvement of statistical properties. Finally, we show that the 2D analytic signal allows for an improved estimation of local features on B-mode images.

1 Introduction

The analytic signal (AS) enables to extract local, low-level features from images. It has the fundamental property of split of identity, meaning that it separates qualitative and quantitative information of a signal in form of the *local phase* and *local amplitude*, respectively. These quantities further fulfill invariance and equivariance properties [11], allowing for an extraction of structural information that is invariant to brightness or contrast changes in the image. Exactly these properties lead to a multitude of applications in computer vision and medical imaging, such as registration [5,15,20,26,31,33], detection [10,21,25,29], segmentation [1,16,27], and stereo [13]. Phase-based processing is particularly interesting for ultrasound images because they are affected by significant brightness variations [15,16,20,21,26].

For 1D, the local phase is calculated with the 1D analytic signal. For 2D, several extensions of the analytic signal are proposed, with the *monogenic signal* [11] presenting an isotropic extension. The description of the signal's structural information (phase and amplitude) is extended by a geometric component, the *local orientation*. The local orientation indicates the orientation of intrinsic 1D (i1D) structures in 2D images. This already points to the limitation of the monogenic signal; it is restricted to the subclass of i1D signals. Recently, an extension to the monogenic signal, referred to as *2D analytic signal* [28], was proposed that
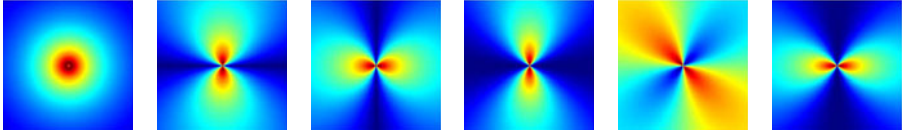
Fig. 1. Magnitude of 2D Hilbert transforms with log-Gabor kernels in frequency domain. From left to right: B, $B \odot H_x^1$, $B \odot H_y^1$, $B \odot H_{xx}^2$, $B \odot H_{xy}^2$, $B \odot H_{yy}^2$.

permits the analysis of i2D signals. Therefore, the 2D signal analysis is embedded into 3D projective space, and a new geometric quantity, the *apex angle*, is introduced. The 2D analytic signal also has the advantage of more accurately estimating local features from i1D signals [28].

In this article, we show the advantages of the calculation of the 2D analytic signal for radio frequency (RF) and B-mode ultrasound images. Instead of performing the demodulation of RF signals for each scan line separately, we perform the demodulation in its 2D context with 2D Hilbert filters of first- and second-order. This leads to advantages in the envelope detection. Since all further processing steps of the creation of the B-mode image are based on the envelope, the improvement of the 2D envelope detection propagates to the quality of the B-mode image. Moreover, the result from the 2D envelope detection bears better statistical properties, as we illustrate with goodness-of-fit tests towards a Nakagami distribution, with its implications to classification and segmentation. Finally, we show the advantages of the 2D analytic signal for estimating local features on B-mode images. All experiments are performed on clinical ultrasound images.

2   2D Analytic Signal

There are various concepts to analyze the phase of signals, such as Fourier phase, instantaneous phase, and local phase [14]. We are primarily interested in the last two. For 1D signals, $g \in L^2(\mathbb{R})$, the instantaneous phase is defined as the argument of the analytic signal, $\arg(g + i \cdot \mathcal{H}\{g\})$, with $\mathcal{H}$ being the Hilbert transform. Since real signals consist of a superposition of multiple signals of different frequencies, the instantaneous phase, although local, can lead to wrong estimates. The signal has to be split up into multiple frequency bands, by means of bandpass filters, to achieve meaningful results, as further described in section 2.2.

Considering 2D signals, $f \in L^2(\mathbb{R}^2)$, the intrinsic dimension expresses the number of degrees of freedom to describe local structures [32]. Intrinsic zero dimensional (i0D) signals are constant signals, i1D signals are lines and edges, and i2D are all other patterns in 2D. The monogenic signal is restricted to i1D signals. The monogenic signal is calculated with the two-dimensional Hilbert transform, also referred to as the Riesz transform. In the frequency domain, the first-order 2D Hilbert transform is obtained with the multiplication of

$$H_x^1(\mathbf{u}) = i \cdot \frac{x}{||\mathbf{u}||}, \quad H_y^1(\mathbf{u}) = i \cdot \frac{y}{||\mathbf{u}||}, \quad \mathbf{u} = (x, y) \in \mathbb{C}\backslash\{(0,0)\} \qquad (1)$$

with $i = \sqrt{-1}$. For the calculation of the 2D analytic signal, higher order Hilbert transforms are used [28]. The Fourier multipliers of the second-order Hilbert transform [1] are

$$H_{xx}^2(\mathbf{u}) = -\frac{x \cdot x}{||\mathbf{u}||^2}, \quad H_{xy}^2(\mathbf{u}) = -\frac{x \cdot y}{||\mathbf{u}||^2}, \quad H_{yy}^2(\mathbf{u}) = -\frac{y \cdot y}{||\mathbf{u}||^2}, \qquad (2)$$

again with $\mathbf{u} = (x, y) \in \mathbb{C}\backslash\{(0,0)\}$. In contrast to [28], we do not present the formulas of the Hilbert transforms in spatial but in frequency domain, which is more versatile for filtering, see section 2.2. Throughout the article we use upper case letters for filter and signals in frequency domain, and lower case ones for their representation in spatial domain.

2.1   Structural and Geometrical Features

The proposed extension of the 2D analytic signal is obtained by an embedding in 3D projective space. This allows for a differentiation of geometrical features (local orientation, local apex) and structural features (local phase, local amplitude). The filtered signal F_p, the first-order Hilbert transformed signals F_x, F_y, and the second-order Hilbert transformed signals F_{xx}, F_{xy}, F_{yy} are calculated with the bandpass filter B and the pointwise multiplication $\odot$ in frequency domain as

$$\begin{bmatrix} F_p \\ F_x \\ F_y \end{bmatrix} = \begin{bmatrix} B \odot F \\ H_x^1 \odot B \odot F \\ H_y^1 \odot B \odot F \end{bmatrix} \quad \text{and} \quad \begin{bmatrix} F_{xx} \\ F_{xy} \\ F_{yy} \end{bmatrix} = \begin{bmatrix} H_{xx}^2 \odot B \odot F \\ H_{xy}^2 \odot B \odot F \\ H_{yy}^2 \odot B \odot F \end{bmatrix}. \qquad (3)$$

We illustrate the Hilbert transforms in frequency domain multiplied with log-Gabor bandpass filters in figure 1. In order to enable an interpretation of second-order Hilbert transformed signals in projective space, an isomorphism between the Hesse matrix and a vector valued representation is used [28], leading to $f_s = \frac{1}{2}[f_{xx} + f_{yy}]$, $f_+ = f_{xy}$, and $f_{+-} = \frac{1}{2}[f_{xx} - f_{yy}]$.

Finally, the local features are calculated as follows. The apex angle α, which differentiates between features of different intrinsic dimensionality, is
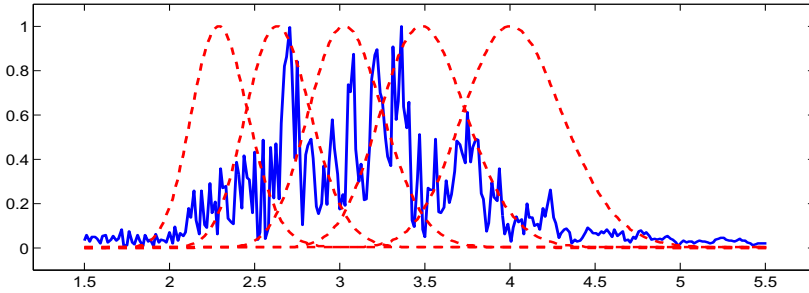
$$\alpha = \arccos \frac{\sqrt{f_+^2 + f_{+-}^2}}{||f_x||}. \qquad (4)$$

With the apex angle, the homogeneous signal component f_h of the signal f_p in projective space is defined as

$$f_h = \sqrt{\frac{1 + \cos\alpha}{2}}. \qquad (5)$$

---

[1] We thank the authors of [28] for discussions and comments on the correct formulas.

Fig. 2. Log-Gabor filter bank consisting of 5 filters (red) and ultrasound signal spectrum (x-axis: frequency in MHz). Ultrasound acquisition frequency: 3.3 MHz.

The local orientation θ, local phase ϕ, and local amplitude a are calculated with

$$\theta = \frac{1}{2} \arctan \frac{f_+}{f_{+-}}, \tag{6}$$

$$\phi = \text{atan2} \left(\sqrt{[f_h^{-1} f_x]^2 + [f_h^{-1} f_y]^2}, f_p \right), \tag{7}$$

$$a = \frac{1}{2} \sqrt{f_p^2 + [f_h^{-1} f_x]^2 + [f_h^{-1} f_y]^2}. \tag{8}$$

For i1D signals, the homogeneous component is $f_h = 1$, and the formulas above reduce to the ones known from the monogenic signal.

2.2 Frequency Selection

Each signal f can be described with the Fourier series, decomposing the signal into components of different frequencies, each one having its own phase and amplitude. The direct application of the Hilbert transform on the original signal, which presents an accumulation of local signals from different frequencies, does therefore not adequately extract local features. Theoretically, we would need to calculate the analytic signal for infinitely narrow bandwidths, *i.e.*, Dirac deltas in the frequency domain. Following the uncertainty principle this results in filters with global support. Bandpass filters present appropriate approximation for a localization in spatial and frequency domain.

Felsberg *et al.* [11] apply the difference of Poisson kernels for frequency selection. An interesting property of the Poisson filter is that it creates a linear scale-space [12]. Another filter that is commonly applied, especially in ultrasound, is the log-Gabor filter [4,15,16,21,26]. Also in our analysis on ultrasound images, we achieved better results with the log-Gabor filter so that we concentrate on it in the following. A drawback of the log-Gabor filter is, however, that it has no analytic expression in the spatial domain. This is also the reason why we presented the Hilbert transforms in equations (1) and (2) in frequency and not in spatial domain, as it is done in [28].

Fig. 3. Exemplar ultrasound processing pipeline for RF to B-mode conversion

Important for the design of the filter bank is to create filters, so that the transfer function of each filter overlaps sufficiently with its neighbors, in order to have a uniform coverage of the spectrum. A filter bank with five log-Gabor filters is illustrated in figure 2. A study of alternative bandpass filters is presented in [4]. For the further analysis, it is either possible to focus on the signal at one specific scale, or accumulate all responses from various scales, as it is *e.g.* done for the phase congruency [19].

3   2D Analytic Signal on RF Ultrasound

The pipeline of the RF to B-mode conversion consists of multiple steps, including amongst others demodulation, non-linear intensity mapping, and filtering [17,30], see figure 3. The demodulation is one of the central parts and extracts the information-bearing signal from a modulated carrier wave. In ultrasound processing, the demodulation is commonly performed by an *envelope detection*. Hereby, the amplitude of the analytic signal is calculated for each of the 1D scan lines separately. Interestingly, calculating the amplitude of the 1D analytic signal is equivalent to the *instantaneous amplitude*. In the literature of ultrasound imaging, it is noted that the quality of ultrasound images can be increased by multi-frequency decomposition and compounding of the received signal, simply referred to as *frequency compounding* [6]. This is equivalent to the *local amplitude* estimation. This constitutes an interesting analogy, between the advantages of the frequency compounded signal to the normal one, on the one hand, and the advantage of the local amplitude in comparison to the instantaneous amplitude, on the other hand. We have neither seen this analogy noted in the literature before, nor the application of local amplitude and local phase techniques to RF data.

In contrast to the usually separate processing of each scan line, we consider all scan lines at once and construct the 2D analytic signal to estimate the local amplitude. This enables an improved envelope detection because the signal is analyzed in its 2D context by also considering information in lateral direction. The balance between influence from lateral and axial direction can be adjusted by the bandwidth in each direction of the bandpass filter, where the smaller spacing in axial direction should be considered accordingly.

3.1   Envelope and B-Mode Results

We perform experiments on multiple RF images acquired from the neck with a linear transducer at 3.3 MHz. The sampling frequency of the RF data is 40 MHz. We compare the envelope detection for: i) 1D analytic signal (AS), ii) 1D analytic

(a) 1D AS   (b) 1D ASF   (c) 2D AS   (d) 2D ASF
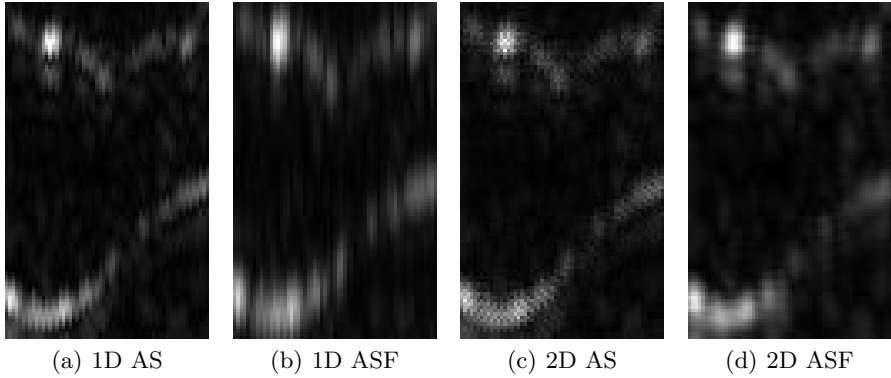
Fig. 4. Magnified region of envelope detected 2D image for various envelopes

(a) 1D AS   (b) 1D ASF   (c) 2D AS   (d) 2D ASF
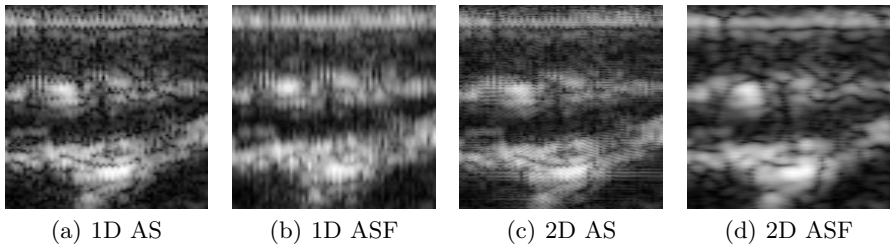
Fig. 5. Magnified regions of images after log-compression

signal with filter bank (ASF), iii) monogenic signal (MS), and iv) monogenic signal with filter bank (MSF), v) 2D AS, and vi) 2D ASF. Exemplarily, we show the frequency spectrum of one scan line together with the log-Gabor filter bank in figure 2. We present magnified regions of the various envelope images in figure 4. Note that we do not show the results of the MS due to limitation of space and better results for 2D AS. However, we include them into the analysis of noise statistics in section 3.2. We can clearly observe that the 2D analytic signal leads to a more accurate and consistent extraction of structures. This becomes particularly clear on the circular structure on the top left, which appears rather ellipsoidal on the estimates from the 1D analytic signal. We also note the positive influence of the filter bank for the estimation of the 2D analytic signal.

We perform an RF to B-mode conversion of local amplitude images a with a log-compression including a translation of 25, $\log(a + 25)$. The results for the various envelopes are presented in figure 5. The B-mode image resulting from the 2D analytic signal clearly shows more consistent structures and less noise. Typically, further filtering steps are applied to the log-compressed image to improve its visual appearance. These processing steps are proprietary to the manufacturer and generally not publicly accessible. Ultrasonix (Redmond, Canada), however, distributes a particular research system with a specific SDK including their post-processing filter, called MUCRO. We apply MUCRO to the

(a) 1D AS   (b) 1D ASF   (c) 2D AS   (d) 2D ASF
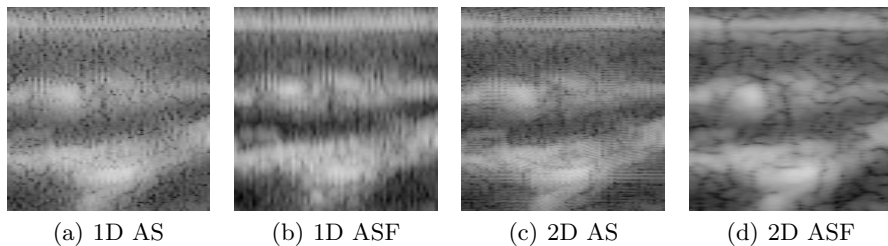
Fig. 6. Magnified regions of images after log-compression and MUCRO

log-compressed images, with the results shown in figure 6. Even after the application of MUCRO, the advantages of the images from the 2D analytic signal are clearly visible. This is not self-evident because the post-processing methods are designed to be applied to 1D envelope detected images, still leaving room for improvement by adapting the post-processing to 2D envelope estimation. Finally, one of the reasons for applying the post-processing filtering is to establish consistency between scan lines, which we already achieve by the 2D envelope detection.

3.2   Analysis of Envelope Statistics

Next to the visual assessment of the 2D envelope detection, we also analyze the statistical properties of the data. Different statistical models have been proposed to model ultrasound data. Among them there is Rician [23], pre-Rician K [18], Generalized K-distribution, homodyned K-distribution as well as Rician Inverse of the Gaussian [9]. Common to all these distributions is the inherent complexity, limiting its practical applicability. In order to address this issue, the Nakagami distribution [22] was proposed, because it admits an explicit analytical expression. It is used in various applications to model backscatter characteristics of US envelope data for segmentation and classification, see [8,24] and references therein. In the following, we analyze the effects of the 2D envelope detection on the speckle statistics choosing the Nakagami model. In particular, we quantify the impact of the 2D analytic signal with goodness-of-fit (GOF) tests, and show the potential for the aforementioned applications based on example images.

The Nakagami distribution $\mathcal{N}(x \mid \mu, \omega)$ belongs to the exponential family and is controlled by two parameters, μ and ω, specifying shape and scale respectively

$$\mathcal{N}(x \mid \mu, \omega) = \frac{2\mu^\mu x^{2\mu-1}}{\Gamma(\mu)\omega^\mu} \exp\left(-\frac{\mu}{\omega}x^2\right), \forall x \in \mathbb{R}_+. \tag{9}$$

A goodness-of-fit test evaluates if the data $d_1, \ldots, d_n$, under the assumption of i.i.d. samples, comes from the given theoretical probability distribution p [7]. Note that conventional GOF tests are restricted to the case of single distributions. For inhomogeneous regions in the image, however, a mixture of Nakagami is more appropriate, see figure 8 for an illustration of a misfit of a single Nakagami to mixture Nakagami data as well as a perfect mixture fit. Consequently,

(a) Neck Image with Sample Distributions   (b) Boxplot of P-Values
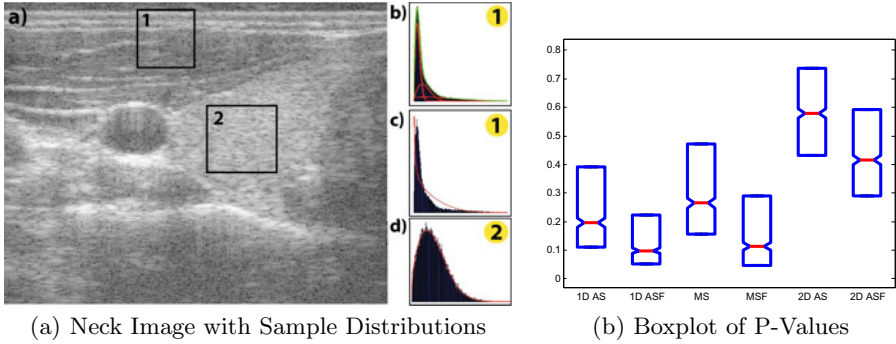
Fig. 7. Left: RF image and distribution estimation of two areas. Region 1 contains a mixture of Nakagami, region 2 a single Nakagami. Whereas MLE can fit nicely in region 2 (d) it expectedly performs poorly in region 1 (c), that can only be represented properly by mixture (b). Right: Box plot of P-values for different envelope detections.

we can only achieve good results with the GOF test on homogeneous image regions. The mixture case has to be further evaluated, with similar results to be expected.

For the GOF test, the range of the data is partitioned into M bins β_i, $i = 1, \ldots, M$, with N_i and the number of samples per bin. Moore [7] suggests to divide the data into $M = 2n^{\frac{2}{5}}$ bins. Furthermore, we assume the bins to be equiprobable as suggested in [3]. In this regard, we let p_i be the integral of the distribution in the range β_i given the parameters of the distribution $\theta = \{\mu, \omega\}$

$$p_i = \int_{\beta_i} p(x \mid \theta)dx. \tag{10}$$

Hence, p_i expresses the likelihood of a sample to be in the bin β_i (identical for all bins). The test statistics underlying the GOF test is the sum of differences between observed and expected outcome frequencies

$$X^2 = \sum_{i=1}^{M} \frac{N_i - np_i}{np_i}. \tag{11}$$

This yields a quadratic form in N_i that has approximately a χ distribution with $M - N - 1$ degrees of freedom and $N = 2$ the number parameters of the distribution. In order to assess the GOF quantitatively, we employ the P-value bases hypothesis test. The P-value serves as an indicator of how likely the null hypothesis H_0 is true. In our case, H_0 is the hypothesis that the observations are Nakagami distributed, leading to the following calculation of the P-value

$$P = \int_{X^2}^{\infty} \chi^2(M - N - 1)dx, \tag{12}$$

employing equation (11) as the lower bound of integration.

(a) 1D AS   (b) 1D ASF   (c) MS   (d) MSF   (e) 2D AS   (f) 2D ASF
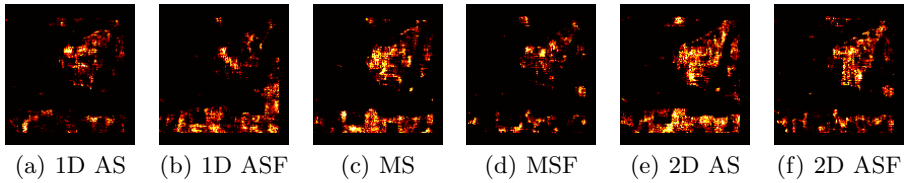
Fig. 8. The P-values are calculated for all patches of an envelope image. Pixel brightness indicates P-value. We perform the calculation for various envelope detection techniques. Comparing the P-value images to the B-mode image in figure 7(a), we see that the bright regions correspond to homogeneous regions in the US image.

3.3 Rao-Robson Statistic

Given the data, we first have to estimate the parameters μ, ω of the Nakagami distribution before the GOF test is performed. This is, however, opposing the general assumption that the parameters of the distribution are a-priori given before the test is performed. Therefore, another quadratic form in N_i has to be used, with the Rao-Robson statistic being one possibility [7]. Considering the parametric form of the distribution $p(x|\theta)$ and the maximum likelihood estimate $\hat{\theta}$, the Rao-Robson statistic is

$$RR = V^\top(\hat{\theta})Q(\hat{\theta})V(\hat{\theta}) \tag{13}$$

with

$$V(\theta) = \frac{N_i - np_i}{(np_i)^{1/2}} \tag{14}$$

$$Q(\theta) = I + D(\theta)[J(\theta) - D^\top(\theta)D(\theta)]^{-1}D^\top(\theta) \tag{15}$$

$$D_{ij}(\theta) = p_i(\theta)^{\frac{1}{2}}\frac{\partial p_i(\theta)}{\partial \theta_j} \tag{16}$$

$J(\theta)$ is the $N \times N$ Fisher information matrix and I is an $M \times M$ identity matrix. The Rao-Robson statistic is χ^2 distributed with $M - N - 1$ degrees of freedom, leading to P-values computed using

$$P = \int_{RR}^\infty \chi^2(M - N - 1)dx \tag{17}$$

with the Rao-Robson statistic RR as lower bound of integration.

3.4 Statistical Results

We perform the Rao-Robson GOF test on local patches of size 180×20, densely throughout the image. Plotting the results for all patches, creates therefore a new image with the intensity values being the P-values. We show these images in figure 8 for the various envelope detections. The brighter the images, the

higher the P-values, and consequently the better for statistical applications because we achieve better fits. We note that the bright regions are corresponding to the homogeneous areas in the ultrasound image because only these areas are appropriately modeled with a single distribution, as discussed previously. Additionally, we calculate the statistics of the P-values, visualized in the box plot of figure 7(b). The red line indicates the median and the box is constructed from the interquartile range. Our results therefore show that the envelope detection without the filter bank produces better fits, which makes sense, because log-Gabor filters influence the distribution. More importantly, however, we note the improvement from 1D AS to MS, and further from MS to 2D AS. This shows on the the one hand, the advantage of applying 2D Hilbert transforms in contrast to 1D ones, and on the other hand, the advantage of the 2D analytic signal in contrast to the monogenic signal. This confirms the visually improved results for 2D envelope detection from the previous section.

4   2D Analytic Signal on B-Mode Images

Next to the benefits of the 2D analytic signal for the demodulation of RF data, it also allows for a more accurate estimation of local features on B-mode images [28]. This has the potential to increase the quality of follow-up applications such as registration [15,20,26,33], segmentation[16], and detection [21], that use the local features as input. To demonstrate this, we calculate the local orientation on B-mode images showing a biopsy needle. In figure 9, we illustrate the local orientation that is estimated from the monogenic signal and the 2D analytic signal, both with filtering. The estimation from the monogenic signal shows no consistent orientation information in the region of the needle. In contrast, the improved concept of the 2D analytic signal indicates a consistent result.
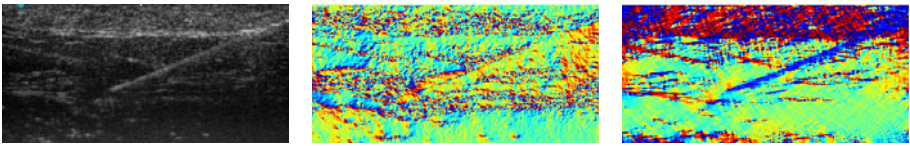
Fig. 9. Ultrasound image with biopsy needle (left). Calculated local orientation for monogenic signal (middle) and 2D analytic signal (right).

5   Conclusion

We demonstrated that the application of the 2D analytic signal has multiple advantageous for RF and B-mode data. The demodulation of RF signals with the 2D analytic signal enables a more consistent extraction of structures, because the signal is analyzed in its natural 2D context. We further showed that the improved envelope detection enables the creation of B-mode images of enhanced quality. To validate this, we applied a proprietary post-processing filtering for

ultrasound on the log-compressed images and compared the result of 1D and 2D analytic signal. Moreover, we validated the improved statistical properties of envelope data resulting from the 2D analytic signal by performing goodness-of-fit tests to a Nakagami distribution. Finally, the advanced signal model of the 2D analytic signal leads to benefits in the estimation of local features in B-mode images, as we have illustrated for the case of needle detection.

For the demodulation, we focused on scans from a linear transducer. For curved linear transducers, the application of 2D Hilbert transforms without a previous scan conversion can be achieved with the polar Fourier transform [2].

References

1. Ali, R., Gooding, M., Christlieb, M., Brady, M.: Advanced phase-based segmentation of multiple cells from brightfield microscopy images. In: ISBI (2008)
2. Averbuch, A., Coifman, R., Donoho, D., Elad, M., Israeli, M.: Fast and accurate polar Fourier transform. Applied and Computational Harmonic Analysis 21(2), 145–167 (2006)
3. Bock, R.K., Krischer, W.: The Data Analysis Briefbook, 1st edn. Springer-Verlag New York, Inc., Secaucus (1998)
4. Boukerroui, D., Noble, J., Brady, M.: On the Choice of Band-Pass Quadrature Filters. Journal of Mathematical Imaging and Vision 21(1), 53–80 (2004)
5. Carneiro, G., Jepson, A.D.: Phase-based local features. In: Heyden, A., Sparr, G., Nielsen, M., Johansen, P. (eds.) ECCV 2002. LNCS, vol. 2350, pp. 282–296. Springer, Heidelberg (2002)
6. Cincotti, G., Loi, G., Pappalardo, M.: Frequency decomposition and compounding of ultrasound medical images with wavelet packets. IEEE Transactions on Medical Imaging 20(8), 764–771 (2001)
7. D'Agostino, R., Stephens, M.: Goodness-of-fit techniques, p. 560. Marcel Dekker, Inc., New York (1986)
8. Destrempes, F., Meunier, J., Giroux, M.F., Soulez, G., Cloutier, G.: Segmentation in ultrasonic b-mode images of healthy carotid arteries using mixtures of nakagami distributions and stochastic optimization. IEEE Trans. Med. Imaging 28(2), 215–229 (2009), `http://dx.doi.org/10.1109/TMI.2008.929098`
9. Dutt, V., Greenleaf, J.F.: Ultrasound echo envelope analysis using a homodyned k-distribution signal model. Ultrason. Imag. 16(4-5), 265–287 (1994)
10. Estépar, R.S.J., Washko, G.G., Silverman, E.K., Reilly, J.J., Kikinis, R., Westin, C.-F.: Accurate airway wall estimation using phase congruency. In: Larsen, R., Nielsen, M., Sporring, J. (eds.) MICCAI 2006. LNCS, vol. 4191, pp. 125–134. Springer, Heidelberg (2006)
11. Felsberg, M., Sommer, G.: The monogenic signal. IEEE Transactions on Signal Processing 49(12), 3136–3144 (2001)
12. Felsberg, M., Sommer, G.: The monogenic scale-space: A unifying approach to phase-based image processing in scale-space. Journal of Mathematical Imaging and Vision 21(1), 5–26 (2004)
13. Fleet, D., Jepson, A., Jenkin, M.: Phase-based disparity measurement. CVGIP: Image Understanding 53(2), 198–210 (1991)

14. Granlund, G.H., Knutsson, H.: Signal Processing for Computer Vision. Kluwer Academic Publishers, Dordrecht (1995)
15. Grau, V., Becher, H., Noble, J.: Registration of multiview real-time 3-d echocardiographic sequences. IEEE Transactions on Medical Imaging 26(9), 1154–1165 (2007)
16. Hacihaliloglu, I., Abugharbieh, R., Hodgson, A.J., Rohling, R.: Bone segmentation and fracture detection in ultrasound using 3D local phase features. In: Metaxas, D., Axel, L., Fichtinger, G., Székely, G. (eds.) MICCAI 2008, Part I. LNCS, vol. 5241, pp. 287–295. Springer, Heidelberg (2008)
17. Hedrick, W.R., Hykes, D.L., Starchman, D.E.: Ultrasound Physics and Instrumentation, 4th edn., Mosby (2004)
18. Jakeman, E., Pusey, P.N.: A model for non-rayleigh sea echo. IEEE Trans. Antennas Propag. 24(4-5), 806–814 (1976)
19. Kovesi, P.: Image features from phase congruency. Videre: Journal of Computer Vision Research 1(3) (1999)
20. Mellor, M., Brady, M.: Phase mutual information as a similarity measure for registration. Medical Image Analysis 9(4), 330–343 (2005)
21. Mulet-Parada, M., Noble, J.: 2D+ T acoustic boundary detection in echocardiography. Medical Image Analysis 4(1), 21–30 (2000)
22. Nakagami, N.: The m-distribution, a general formula for intensity distribution of rapid fadings. In: Hoffman, W.G. (ed.) Statistical Methods in Radio Wave Propagation, Pergamon, Oxford (1960)
23. Shankar, P.M., Reid, J.M., Ortega, H., Piccoli, C.W., Goldberg, B.B.: Use of non-rayleigh statistics for the identification of tumors in ultrasonic b-scans of the breast. IEEE Trans. Med. Imag. 12(4-5), 687–692 (1993)
24. Shankar, P., Dumane, V., Reid, J., Genis, V., Forsberg, F., Piccoli, C., Goldberg, B.: Classification of ultrasonic b-mode images of breast masses using nakagami distribution. IEEE Transactions on Ultrasonics, Ferroelectrics and Frequency Control 48(2), 569–580 (2002)
25. Szilágyi, T., Brady, S.M.: Feature extraction from cancer images using local phase congruency: a reliable source of image descriptors. In: ISBI, pp. 1219–1222 (2009)
26. Wachinger, C., Navab, N.: Alignment of viewing-angle dependent ultrasound images. In: Yang, G.-Z., Hawkes, D., Rueckert, D., Noble, A., Taylor, C. (eds.) MICCAI 2009. LNCS, vol. 5761, pp. 779–786. Springer, Heidelberg (2009)
27. Wang, P., Kelly, C., Brady, M.: Application of 3d local phase theory in vessel segmentation. In: ISBI, pp. 1174–1177 (2009)
28. Wietzke, L., Sommer, G., Fleischmann, O.: The geometry of 2d image signals. In: CVPR, pp. 1690–1697 (2009)
29. Xiaoxun, Z., Yunde, J.: Local Steerable Phase (LSP) Feature for Face Representation and Recognition. In: CVPR, vol. 2 (2006)
30. Zagzebski, J.: Essentials Of Ultrasound Physics, 1st edn., Mosby (1996)
31. Zang, D., Wietzke, L., Schmaltz, C., Sommer, G.: Dense optical flow estimation from the monogenic curvature tensor. In: Scale Space and Variational Methods in Computer Vision, pp. 239–250 (2007)
32. Zetsche, C., Barth, E.: Fundamental limits of linear filters in the visual processing of two dimensional signals. Vision Research (30) (1990)
33. Zhang, W., Noble, J.A., Brady, J.M.: Spatio-temporal registration of real time 3D ultrasound to cardiovascular MR sequences. In: Ayache, N., Ourselin, S., Maeder, A. (eds.) MICCAI 2007, Part I. LNCS, vol. 4791, pp. 343–350. Springer, Heidelberg (2007)